Available online at www.sciencedirect.com
SCIENCE DIRECT®
Journal of Nuclear Materials 321 (2003) 121–128
journal of nuclear materials
www.elsevier.com/locate/jnucmat

Helium behavior in UO_2 polycrystalline disks

S. Guilbert [a,*], T. Sauvage [a], H. Erramli [b], M.-F. Barthe [a], P. Desgardin [a], G. Blondiaux [a], C. Corbel [c], J.P. Piron [d]

[a] *Centre d'Etudes et de Recherches par Irradiation, 45071 Orléans, France*
[b] *Nuclear Physics and Techniques Laboratory, Faculty of Sciences Semlalia, B.P. 2390, University Cadi Ayyad, Marrakech, Morocco*
[c] *Laboratoire de Radiolyse, CEA Saclay, 91191 Gif sur Yvette, France*
[d] *DEN/DEC/SESC, CEA Cadarache, 13108 St Paul Lez Durance, France*

Received 12 August 2002; accepted 7 April 2003

Abstract

The behavior of helium implanted in sintered uranium dioxide disks has been investigated as a function of annealing temperature. UO_2 disks have been implanted with 1 MeV ^3He at a nominal fluence of 5×10^{16} $^3He\,cm^{-2}$ using a Van de Graaff accelerator. The $^3He(d,\alpha)^1H$ nuclear reaction analysis method was used to determine the helium depth profile in the UO_2 disks. Partial flaking was observed after annealing at 500 °C for local He concentration of 1 at.%. After annealing at 600 °C flaking has affected the whole surface. The formation of helium bubbles is discussed.

PACS: 66.30.h; 61.82.m; 81.05.Je

1. Introduction

The release of fission gases, mostly Xe, from UO_2 and spent fuels has been extensively studied since the middle of the 1960s [1–5]. The solubility of these gases is extremely low in UO_2 and, as a consequence, the gas atoms tend to precipitate into bubbles. In irradiated fuels, a high density ($\sim10^{17}$ cm^{-3}) of small intragranular bubbles of about 2 nm uniformly distributed in the matrix are observed [6,7]. The size of the bubbles increases and the concentration decreases slightly with increasing temperature and burnup. At higher burnup and/or temperatures a second bubble population is created with a larger mean diameter (10–20 nm) [7]. The precipitation of bubbles has also been demonstrated for uranium dioxide samples *implanted* with Kr and Xe even at temperatures as low as 300–350 °C [8,9].

Fewer experiments have been performed on the behavior of helium gas produced by alpha decay of actinides [10,11]. Yet the amount of helium produced after irradiation are large in particular in the case of MOX fuels: the amount of helium produced in MOX (burnup 47.5 GWd/tU) after 10 000 years is evaluated at 6700 cm^3 STP per rod – 4% He atoms/initial heavy metal atoms at/at_{iHM}. For comparison, the volume of fission gas generated in irradiation is around 2500 cm^3/rod STP – 1.5% at/at_{iHM} [12,13].

Rare gases can be introduced into solids either by internal fission using reactor irradiation, or by ion implantation or by doping the solid with soluble precursors (e.g. I for Xe) the gas being produced by decay [14]. *Ion implantation* has some advantages compared to the two other techniques. First it involves less experimental constraints avoiding the use of hot cells. Secondly the ion energy and the ion fluence can be varied by many orders of magnitude.

We present, in this paper, the first results we obtained on the behavior of helium in uranium dioxide. Helium was introduced into the UO_2 disks by ion implantation. We used the $^3He(d,\alpha)^1H$ nuclear reaction analysis method to determine the helium depth profile in as-implanted UO_2 sintered disks and after annealing at 500 °C and 600 °C in Ar/H_2 atmosphere. This method is

* Corresponding author. Tel.: +33-2 38 25 54 27; fax: +33-2 38 63 02 71.
E-mail address: severine.guilbert@irsn.fr (S. Guilbert).

0022-3115/$ - see front matter
doi:10.1016/S0022-3115(03)00212-5

used here in an original way where both emitted particles, α and ^1H, are detected in coincidence with in addition the proton detected in the transmission mode. Although this coincidence technique results in a significant increase in the counting time, it has the advantage to suppress nearly all parasite signals. The resulting signal in this coincidence mode has such a quality that the He profile can be achieved with a much better resolution than in a single detection mode.

2. Experimental details

2.1. Sample preparation

Sintered uranium dioxide disks (0.2 at.% ^{235}U) have been used for this study. The mean grain size is 8 μm and the mean O/U ratio determined by polarography is 2.0083 ± 0.0060. The density of the material is 10.46 ± 0.03 g cm^{-3}. The disks are 300 μm thick and 8.2 mm in diameter. After polishing of one side, the disks were annealed at 1300 °C under H_2 for 1 h to remove polishing damage.

2.2. The $^3He^+$ implantation

Four UO_2 disks (E1, E2, E3, E4) have been implanted under vacuum ($P = 5 \times 10^{-6}$ mbar) with 1 MeV ^3He using the 3.5 MV Van de Graaff accelerator at CERI Orléans. The implantation is performed by focusing the beam (1×1 mm^2) and by sweeping it over the disk surface to ensure a homogeneous dose. The four disks of uranium dioxide were implanted during the same run at a nominal fluence of 5×10^{16} $^3He^+$ cm^{-2}. One disk was kept as-implanted (E1) and the three others were annealed after implantation.

2.3. High temperature annealing under H_2/Ar

Annealings were performed at two temperatures, 500 and 600 °C, for 1 h in 10 vol.% H_2/Ar atmosphere. The E2 and E3 disks have been annealed at 500 °C and the E4 disk has been annealed at 600 °C. The atmosphere of the furnace was purged of oxygen before annealing by H_2/Ar sweeping for 1 h. The heating step takes approximately 45–50 min. At the end of the heating step, H_2/Ar was maintained in the furnace approximately 15 h during the cooling of the disks down to 30 °C in order to prevent oxidation of the disk surface.

2.4. Surface state and helium lateral and depth distribution

Different techniques have been used to characterize the surface state of the disks and the helium lateral distribution and depth profile.

2.4.1. Surface analysis

The surface state of the as-received, as-implanted and annealed disks have been observed using a binocular magnifying glass (Leika) and a Philips (XL40) Environmental Scanning Electron Microscope (ESEM, 30 kV, partial pressure of air $\sim 2 \times 10^{-3}$ atm) from Ernest Babelon Laboratory (CNRS Orléans).

The roughness of the disks after implantation and annealing was measured using a Talysurf 10 (Taylor-Hobson).

2.4.2. Helium depth profile and lateral distribution

Several methods based on ion beams can be used to determine the total amount of helium in solids. Among these methods, the $^3He(d,\alpha)^1H$ nuclear reaction analysis method is widely known [15–18]. In this study we used this technique in different conditions depending on the type of information we wanted to obtain.

Homogeneity of the lateral implanted helium distribution is investigated by performing cartography of the disk surface. In this analysis mode, the spot of the deuteron beam is moved by step of 250 μm on either side from the disk center and only protons transmitted through the sample are detected at 0° angle from the incident deuteron beam. The lateral resolution is restricted to 500×500 μm^2 due to the spot size of the deuteron beam.

For helium depth profiling, the two reaction products, ^1H and α, are detected in coincidence in order to suppress all parasite signal. The details of the method (analysis set-up, $^3He(d,\alpha)^1H$ cross section data, energy calibration mode of detectors ...) are reported elsewhere [18]. A deuteron energy of 768 keV is chosen in order to have the maximum of the cross section at the 2 μm projected range of 1 MeV ^3He in UO_2 and to obtain the highest detection limit. For this large range of implantation depth, the depth resolution of helium profile in UO_2 is close to 0.1 μm.

The He depth profile was then determined from the α experimental spectra using the $^3He(d,\alpha)^1H$ cross section measured by Sauvage et al. given in [19] and the SIMNRA program [20] in which the Ziegler–Biersack–Littmark (ZBL) stopping powers were integrated [21]. This program fits the experimental data assuming a sequence of uranium dioxide layers with different He concentrations.

3. Results and data analysis

The as-implanted (E1) and the annealed disks (E2, E3, E4) have been characterized by optical microscopy, ESEM and NRA.

3.1. Optical and electronic microscopy

Fig. 1(a) is typical of the surface state observed by optical microscopy on a scale of 1–44 in the as-received

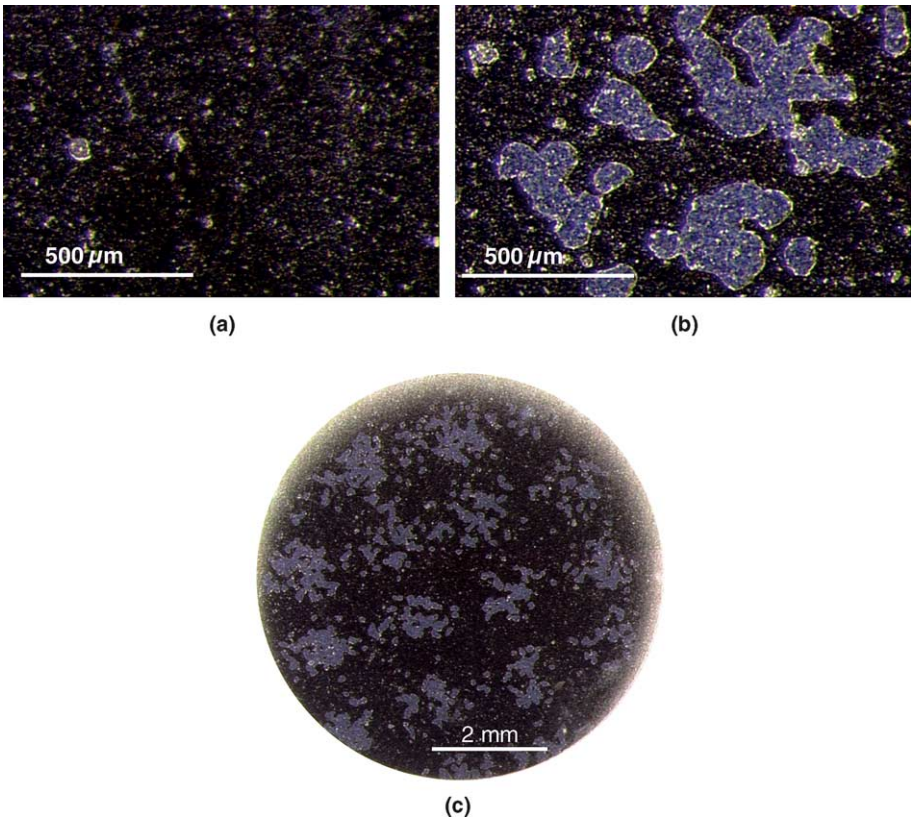

Fig. 1. Binocular image of (a) He-implanted UO_2 E1 disk, (b) and (c) He-implanted UO_2 E2 disk after annealing at 500 °C/1 h/H_2.

as well as in the as-implanted uranium dioxide disks. It shows that the implantation induces no modification of the surface state.

After annealing at 500 °C, as shown in Fig. 1(b) the appearance of bright zones surrounded by dark zones at the surface of the E2 disk can be detected by optical microscopy on a scale of 1–57. They have different shapes ranging from tens to hundreds of μm. As shown in Fig. 1(c) on a scale of 1–8, the largest bright zones appear as small islands regularly distributed in a square lattice of 2 mm parameter. The dark zones look like the surface of the as-implanted E1 disk. The same features are observed on the other 500 °C annealed E3 disk. Fig. 2(a) shows that, when observed by ESEM on a scale of 1–260, the dark and the bright zones appear to be sharply delimited. The sharpness of the edge between a dark and a bright zone is better seen on a scale of 1–1900 in Fig. 2(b). Furthermore, the image in Fig. 2(b) clearly points out the existence of a difference in height between these two zones as observed by ESEM, the dark one looking closer to the objective than the bright one.

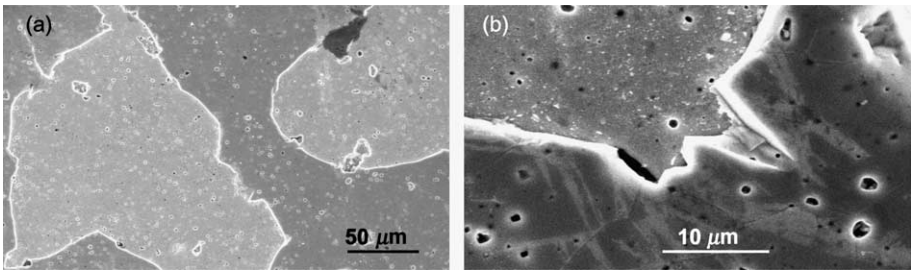

Fig. 2. (a) and (b) ESEM images of He-implanted UO_2 disk after annealing at 500 °C/1 h/H_2 E2.

After annealing at 600 °C, the bright zones cover almost all the disk surface and there is only few dark zones in some places (not shown here). The size of the dark zones ranges from 10 to 100 μm at the most. Edges between dark and bright zones are also observed by ESEM on E4 disk (not shown here).

3.2. Lateral helium distribution

After implantation, as shown in Fig. 3(a), the helium lateral distribution, determined by NRA with a resolution of 500×500 μm^2 due to the beam size, is homogeneous. The proton mean yield is equal to 1244 ± 40 counts for a total deuteron charge of 10 nC/point.

After annealing at 500 °C, Fig. 3(b) shows that heterogeneity in the helium lateral distribution appears on the E2 disk. Different domains of few hundreds of μm wide are observed: domains where the proton yield is the same as the as-implanted E1 disk and domains where the proton yield for a charge of 10 nC/point amounts to roughly one third of the proton yield measured on the as-implanted E1 disk. This heterogeneity in the proton yield is also observed on the E3 disk. Consequently, it can be concluded that annealing at 500 °C induced a strong reduction in the proton yield in some regions of the surface. As shown in Fig. 3(b) these domains of low proton yield appear as islands surrounded by domains with higher proton yield.

After annealing at 600 °C, Fig. 3(c) shows that the helium lateral distribution is homogeneous with a mean proton yield of 158 ± 11 counts for a total charge of 10 nC/point. It is worth mentioning here that in the E4 disk the mean proton yield for the whole area amounts to 13% of the proton yield measured on the as-implanted E1 disk. Consequently, it can be concluded that annealing at 600 °C induced a huge reduction in the mean proton yield.

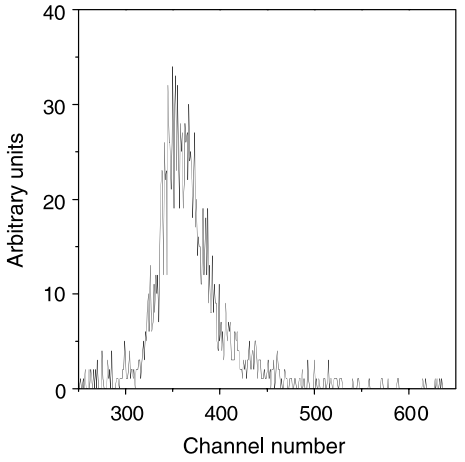

Fig. 4. Experimental NRA spectrum of the as-implanted E1 disk in arbitrary units.

3.3. Helium depth profile

After implantation, as shown in Fig. 4, the experimental NRA spectrum, obtained by detecting the α particles in coincidence with the ^{1}H, presents a sharp peak reaching a maximum at channel ~360. Fig. 5(a) shows that the ^{3}He depth profile deduced from the experimental spectrum measured in the E1 disk exhibits a sharp peak with the ^{3}He concentration reaching a maximum of 1.1 at.%. This maximum is located at a depth of 1.9 μm and the experimental full width at half maximum (FWHM) of the He peak is equal to 0.7 μm. The total He content deduced from this profile amounts to 6.35×10^{16} ^{3}He cm^{-2}. It is worth noting that the He peak is asymmetrical and that a helium tail between the surface and the implantation depth is observed.

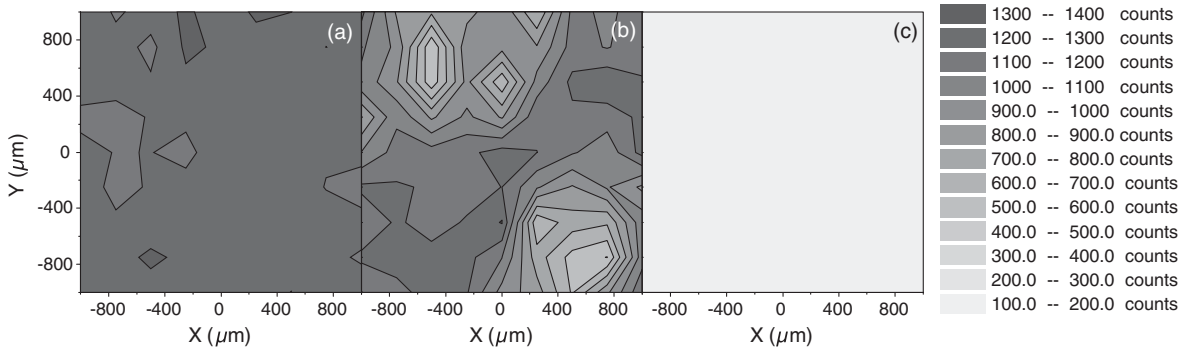

Fig. 3. Lateral helium distribution of implanted disk using proton detection in arbitrary units: (a) as-implanted E1 disk (1 MeV, 5×10^{16} ^{3}He cm^{-2}, $R_p = 2$ μm), (b) implanted disk after annealing at 500 °C/1 h/H_2 E2, (c) implanted disk after annealing at 600 °C/1 h/H_2 E4.

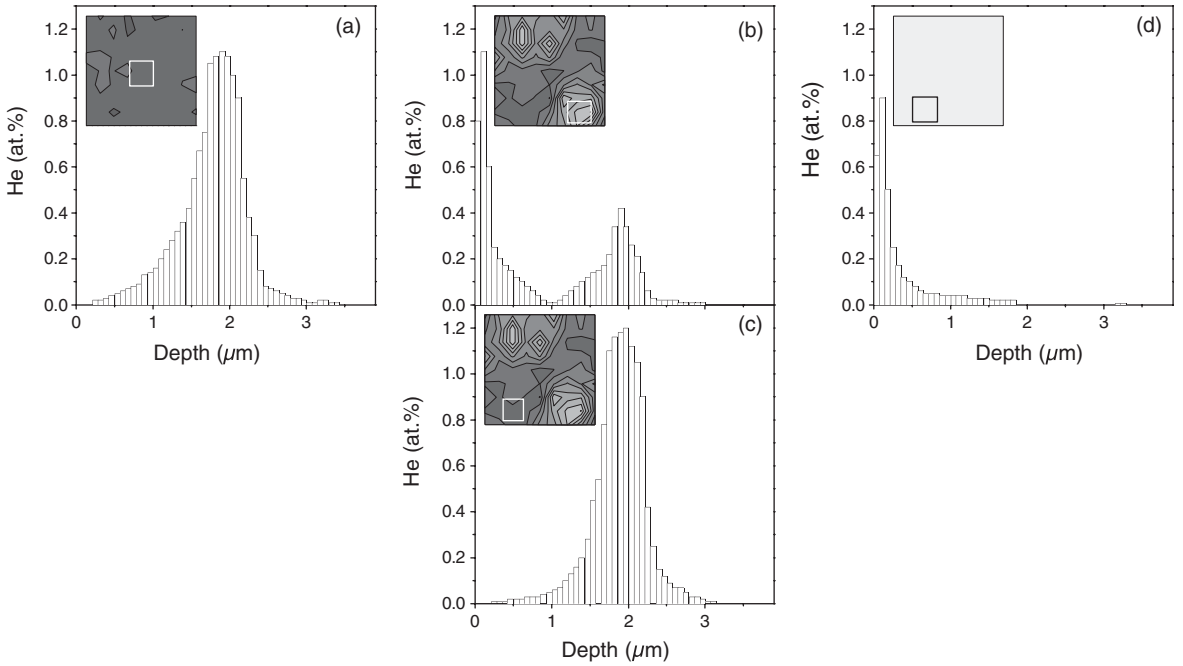

Fig. 5. ^{3}He depth profile in UO_2 (a) as-implanted E1 disk, (b) and (c) implanted disk after annealing at 500 °C/1 h/H_2 E2, (d) implanted disk after annealing at 600 °C/1 h/H_2 E4.

After annealing at 500 °C, as discussed in Section 3.2, the ^{3}He lateral distribution is heterogeneous for both the E2 and E3 disks.

In the domains, identified in Section 3.2, where the proton yield is lower than in the as-implanted disk E1, Fig. 5(b) shows that the helium depth profile determined on the E2 disk exhibits two different peaks. The profile determined on the E3 disk presents the same features (not shown here). For both disks, one peak is located at the near-surface and the other one is at 1.9 μm. The helium concentration at the maximum of the near-surface peak is 1.1 at.% for E2 and 0.9 at.% for E3. The near-surface peak is highly asymmetric extending only towards the bulk of the disk with a FWHM of 0.2 μm. The total helium amount in this near-surface peak, between 0 and 1 μm depth, is equal to 1.85×10^{16} ^{3}He cm^{-2} for E2 and 1.45×10^{16} ^{3}He cm^{-2} for E3. We can notice that for the E2 disk the higher helium concentration at the maximum is linked with a higher total helium amount in the peak. For E3, the smaller helium concentration at the maximum is associated with a smaller total helium amount. The helium concentration at the maximum and the FWHM of the 1.9 μm peak are respectively equal to 0.4 at.% and 0.4 μm for the disk E2, 0.45 at.% and 0.5 μm for E3. Between 1 and 3 μm depth, the total helium amount is equal to 1.5×10^{16} ^{3}He cm^{-2} for E2 and 1.8×10^{16} ^{3}He cm^{-2} for E3. The total amount of helium determined from the profiles obtained amounts to 3.35×0^{16} ^{3}He cm^{-2} for E2 and 3.25×10^{16} ^{3}He cm^{-2} for E3. These values are two times lower than in the as-implanted disk E1.

In the domains, identified in Section 3.2, where the proton yield is the same as in the as-implanted E1 disk, as shown in Fig. 5(c), the peak in the depth profile, the FWHM and the helium concentration at the maximum of the peak are respectively 1.9, 0.6 μm and 1.2 at.% for both disks. The total amount deduced from the two He profiles is equal to $(6.2\pm0.2)\times10^{16}$ ^{3}He cm^{-2}. This value is the same as in the as-implanted disk E1.

After annealing at 600 °C, Fig. 5(d) shows that helium is detected only in the first 1.5 μm depth under the surface and there is no more helium at 1.9 μm. The profile shows a peak near the surface with an He concentration at the maximum of 0.9 at.%. The peak is highly asymmetrical with a FWHM of 0.2 μm and a long tail extending towards the bulk where the helium concentration decreases when probing depth increases. Beyond 1.5 μm, the He content is lower than the detection limit of the technique. The total amount of helium deduced from the profile is equal to 1.7×10^{16} ^{3}He cm^{-2}.

4. Discussion

In this paragraph, the evolution of the He distribution and of the surface state as well as the mechanisms

that are induced by annealing at 500 and 600 °C are discussed.

After implantation, the homogeneity in the lateral helium distribution is consistent with the method used to irradiate the samples. The experimental depth corresponding to the maximum in helium concentration, 1.9 μm, is in good agreement with the depth calculated by SRIM 2000 ($R_p = 2$ μm). Nevertheless the experimental FWHM of the ^{3}He profile is larger than the one calculated using SRIM 2000, 0.7 μm versus 0.45 μm, and the experimental He content at the maximum is lower, 1 at.% versus 1.4 at.% for SRIM calculations.

After annealing at 500 °C, several new features (see Section 3.3) appear pointing out a rearrangement of damage or/and He in the implanted UO_2 disks. By correlating optical or scanning electron microscopies to roughness (Fig. 6) and NRA measurements, we are led to conclude that the bright areas of 150–250 μm lateral dimensions observed by optical microscopy correspond to areas left over when matter has been torn off on a thickness of about 1.6 μm. The tearing of matter is consistent with the presence of uranium dioxide flakes that we found in the furnace when taking out the disks at the end of the 500 °C annealing. The striking feature is that this process appears to be highly inhomogeneous in the disks with the flaked areas surrounded by large unflaked areas where the He distribution is identical to its distribution in the as-implanted zone. Depending on their size, the flaked areas extend from few to several grains of uranium dioxide. Furthermore, on a scale of 1–8, it seems that the flaked areas are ordered and formed a flaked area lattice with a lattice parameter ~2 mm. The heterogeneity of the flaking process after annealing at 500 °C suggests the existence of either an implantation revealed or induced heterogeneity in the UO_2 disks. The absence of modification in the ^{3}He depth profile and the total He amount measured in the dark zones compared to the as-implanted E1 disk points out that in these dark zones there is neither helium release nor migration. On the contrary, in the bright zones where both quantities are strongly modified, there is evidence that defect or He reorganization changes the damage structure. The reason for the heterogeneity in the occurrence of this reorganization remains however unclear.

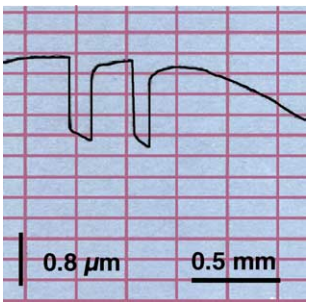

Fig. 6. Roughness measurements performed after implantation and annealing at 500 °C/1 h/H_2 on the disk E2.

After annealing at 600 °C, new features appear: ^{3}He is missing at a depth of 1.9 μm, it is located only at the near-surface and the ^{3}He amount is four times lower than the one measured in the as-implanted E1 disk. Moreover, the whole surface of the E4 disk is seen by optical microscopy as bright as the flaked zones observed in the 500 °C annealed E2 and E3 disks. The correlation between the ^{3}He and surface state evolution suggest that 600 °C annealing induces flaking over the whole surface of E4. Flaking is also confirmed by the weight loss of the E4 disk: the disk annealed at 600 °C has lost approximately 1 mg, which correspond to a UO_2 thickness of 2 μm. After flaking at 600 °C, the ^{3}He content is mostly concentrated in a near-surface peak where the concentration reaches a maximum value of 0.9 at.%. This value is close to the concentration determined at 1.9 μm in the as-implanted E1 disk. This suggests that splitting occurs close to this depth. Surprisingly, however, whereas the helium concentration at the maximum of the peak has hardly changed, the total ^{3}He amount is reduced by a factor of 4. It follows that most of the released ^{3}He comes from the region located before the ion track end. This leads to suggest that splitting is due to some rearrangement in the cascade region involving only short range diffusion of ^{3}He.

Assuming that the ^{3}He properties are the same in the flaked areas after annealing at 500 and 600 °C, it is possible to estimate the surface fraction that has been flaked in the low proton yield areas probed by NRA.

Let $Y_{\text{total 500 °C}}$ be the total amount of helium in the low proton yield area after annealing at 500 °C, $Y_{\text{total 600 °C}}$ the total amount of helium after annealing at 600 °C, $Y_{\text{as-implanted}}$ the total helium amount in the as-implanted disk and f the fraction of flaked area in the low proton yield probed zone (500×500 μm^2).

Then

$$Y_{\text{total 500 °C}} = f \times Y_{\text{total 600 °C}} + (1 - f) \times Y_{\text{as-implanted}} \quad \text{and}$$

$$f = \frac{Y_{\text{as-implanted}} - Y_{\text{total 500 °C}}}{Y_{\text{as-implanted}} - Y_{\text{total 600 °C}}}.$$

So in the low proton yield probed zone, the fraction of flaked areas amounts to 64% for E2 and 62% for E3.

Blistering of metals subjected to helium irradiation has also been intensively investigated [22]. For example, blistering in copper takes place at 320 K during low energy (160 keV) He implantation inducing local He concentration of 30 at.% [22]. Flaking was also observed in oxides: as example in $MgAl_2O_4$ single-crystal after implantation of 900 keV ^{3}He inducing local He con-

centration of 3.8 at.% and subsequent annealing at temperatures higher than 550 °C [23]. It is worth noting that this phenomenon was not observed in the case of polycrystalline $MgAl_2O_4$ where the local He content was only 2.3 at.% [23]. This phenomenon is also successfully used in silicon-on-insulator technology [24–26] to split a thin SiO_2/Si layer from a Si wafer. It involves implantation to high dose ($\sim$1–6$\times10^{16}$ cm^{-2}) of hydrogen ions of low keV energy and subsequent thermal annealing to induce splitting of a layer of material with a thickness comparable to the ion range.

The mechanisms of flaking are well understood [27]: this phenomenon occurs if the implanted gas is unable to escape from the host material. It coalesces and precipitates to form gas filled bubbles. These bubbles may grow by capturing additional gas atoms and vacancies or by punching out interstitial dislocation loops. When they become large enough, a crack parallel to the sample surface will be formed. The layer separated from the substrate by this crack may contain a huge compressive lateral stress. This stress and/or the pressure of the gas accumulated in the cavity formed by the crack lifts covering layer up, deforms it plastically and may even tear it off from the bulk.

It is interesting to notice that in this study, flaking was observed for local He concentration of only 1 at.% (3% at/at$_{iHM}$) whereas this phenomenon is usually observed for at least a few at.%, as example 3.8 at.% in $MgAl_2O_4$ single-crystal [23]. This He concentration would be expected in MOX fuels after 5000 years [12]. It is important to notice that after such a period of time the temperature expected in a geological disposal is less than 200 °C, lower than the temperature of this experiment. At such temperature, the question is whether long aging period can allow a flaking phenomenon similar to the one observed during short annealing at 500 °C.

Finally, these results show that helium bubbles precipitate at temperature as low as 500 °C in uranium dioxide and that the solubility of He in this material (with mean grain size of 8 μm) is less than 1 at.% ($=3\%$ at/at$_{iHM}$).

5. Conclusions

In this work, He behavior after implantation was investigated using nuclear reaction analysis (^{3}He(d,α)^{1}H) as a function of temperature. This study shows that a flaking process of the implanted uranium dioxide occurs for local He concentration of about 1 at.%. This result suggest that the helium solubility is rather low in uranium dioxide. Current work is devoted to the determination of helium diffusion coefficient in medium dose He implanted samples.

Acknowledgements

The authors are grateful to the French electrical utility Électricité de France (EDF) and the Research Program on the long term Evolution of Spent Fuel waste Packages of the CEA (PRECCI) for their financial support. Grateful acknowledgements are made to the members of Ernest Babelon laboratory of the CNRS-Orléans for optical microscopy and ESEM.

References

[1] W. Miekeley, F.W. Felix, J. Nucl. Mater. 42 (1972) 297.
[2] G.T. Lawrence, J. Nucl. Mater. 71 (1978) 195.
[3] P. Lösönen, J. Nucl. Mater. 280 (2000) 56.
[4] J.A. Turnbull, C.A. Friskney, J. Nucl. Mater. 71 (1978) 238.
[5] V.F. Chkuaseli, Hj. Matzke, J. Nucl. Mater. 223 (1995) 61.
[6] R.M. Cornell, J. Nucl. Mater. 38 (1971) 319.
[7] S. Kashibe, K. Une, K. Nogita, J. Nucl. Mater. 206 (1993) 22.
[8] Hj. Matzke, A. Turos, J. Nucl. Mater. 188 (1992) 285.
[9] J.H. Evans, J. Nucl. Mater. 188 (1992) 222.
[10] F. Rufeh, D.R. Olander, T.H. Pigford, Nucl. Sci. Eng. 23 (1965) 335.
[11] P. Sung, Equilibrium solubility and diffusivity of helium in single crystal uranium dioxide, UMI Dissertation Services, University of Washington, USA, PhD, 1967.
[12] J.P. Piron, M. Pelletier, J.C. Dumas, C. Poinssot, J.M. Gras, Spent nuclear fuel evolution in closed system, ASME ICEM'01 Conf., Bruges, Belgium, September 30–October 4, 2001.
[13] C. Poinssot, P. Toulhoat, J.P. Piron, C. Cappelaere, L. Desgranges, J.M. Gras, Operational and scientific questions related to the long term evolution of spent nuclear fuels, ANS Annual Meeting, San Diego CA, USA, June 4–8, 2000.
[14] Hj. Matzke, Radiat. Eff. 53 (1980) 219.
[15] W. Möller, M. Hufschmidt, D. Kamke, Nucl. Instrum. and Meth. 140 (1977) 157.
[16] M. Hufschmidt, V. Heintze, W. Möller, D. Kamke, Nucl. Instrum. and Meth. 124 (1975) 573.
[17] D. Gosset, P. Trocellier, Y. Serruys, J. Nucl. Mater. 303 (2002) 115.
[18] F. Pászti, Nucl. Instrum. and Meth. B 66 (1992) 83.
[19] T. Sauvage, H. Erramli, S. Guilbert, M.-F. Barthe, P. Desgardin, G. Blondiaux, C. Corbel, J.P. Piron, F. Labohm, A. Van Veen, J. Nucl. Mater., submitted for publication.
[20] M. Mayer, SIMNRA user's guide, technical report IPP 9/113, Forschungszentrum Jülich, Max-Planck-Institut für Plasmaphysik, Jülich, Germany, 1997.
[21] J.F. Ziegler, J.P. Biersack, U. Littmark, The Stopping and Range of Ions in Matters, Pergamon, New York, 1985.
[22] P.B. Johnson, R.W. Thomson, K. Reader, J. Nucl. Mater. 273 (1999) 117.

[23] E.A.C. Neeft, A. van Veen, R.P.C. Schram, F. Labohm, Prog. Nucl. Energy 38 (3–4) (2001) 287.
[24] S.W. Bedell, W.A. Lanford, J. Appl. Phys. 90 (3) (2001) 1138.
[25] C. Qian, B. Terreault, J. Appl. Phys. 90 (10) (2001) 5152.
[26] B. Aspar, H. Moriceau, E. Jalaguier, C. Lagahe, A. Soubie, B. Biasse, A.M. Papon, A. Claverie, J. Grisolia, G. Benassayag, F. Letertre, O. Rayssac, T. Barge, C. Maleville, B. Ghyselen, Electron. Mater. 30 (7) (2001) 834.
[27] F. Pászti, Nucl. Instrum. and Meth. B 62 (1992) 377.